Computational Fluid Dynamics Simulation of Chromia Volatilization and Gas-Phase Evolution during Oxidation of Chromia-Forming Alloy: Cross-Linked Influence of Local Gas Velocity and Confined Geometries

Sharvan Kumar, Hugues Vergnes, Brigitte Caussat, Aurélie Vande Put

▶ To cite this version:

> Sharvan Kumar, Hugues Vergnes, Brigitte Caussat, Aurélie Vande Put. Computational Fluid Dynamics Simulation of Chromia Volatilization and Gas-Phase Evolution during Oxidation of Chromia-Forming Alloy: Cross-Linked Influence of Local Gas Velocity and Confined Geometries. High Temperature Corrosion of Materials, 2025, 102 (4), pp.22. ⟨10.1007/S11085-025-10343-5⟩. ⟨hal-05171923⟩

HAL Id: hal-05171923

https://hal.science/hal-05171923v1

Submitted on 22 Jul 2025

Computational Fluid Dynamics simulation of chromia volatilization and gas phase evolution during oxidation of chromia forming alloy: cross-linked influence of local gas velocity and confined geometries

Sharvan Kumar[a]*, Hugues Vergnes[b], Brigitte Caussat[b] and Aurelie Vande Put[a#]

[a]CIRIMAT, Université de Toulouse, INPT-ENSIACET, 4 allée Emile Monso, BP 44362, 31030 Toulouse Cedex 4, France

[b]LGC, Université de Toulouse, INPT-ENSIACET, 4 allée Emile Monso, BP 44362, 31030 Toulouse Cedex 4, France

***sharvan.kumar@toulouse-inp.fr**

#aurelie.vandeput@toulouse-inp.fr

Abstract

An experimentally validated and self-standing CFD (Computational Fluid Dynamics) model was used to analyse chromia volatilization under high velocity conditions close to industrial applications range, in wet air and pure O_2 environment at 800 and 900°C. A rig of complex geometry with several lined-up samples was designed. The simulations revealed the combined and non-trivial influences of gas phase enrichment from upstream samples, local gas velocity and ratio between sample surface and corresponding free volume for gas flow. The CFD results also validated the often-used analytical approach for single sample planar geometries. For more complex situations, the CFD route is necessary.

Keywords: CFD simulation, Chromia forming alloys, Surface/Volume ratio, Chromia volatilization, High temperature oxidation.

1. Introduction

High temperature metallic alloys generally rely on the formation of a protective oxide layer such as chromia or alumina to maintain a good resistance to high temperature oxidation. The stability of these oxides is a function, among others, of the environment and temperature of exposure. Depending on the temperature and the gas phase composition, gaseous species (such as water vapor, oxygen, chlorine…) can react with the oxide layer to form volatile species [1-7]. This leads to a thinning of the protective scale, an acceleration of the oxidation kinetics and ultimately this speeds up the alloy end of life. In case of chromia forming alloys, significant volatilization occurs over 1000 °C in oxidizing environments characterized by a high oxygen partial pressure [8] and over 600 °C in oxidizing and H_2O-rich atmospheres [9-12]. The reaction between chromia and an oxidizing and H_2O-rich environment results in the formation of various volatile species such as $CrO_2(OH)_2$, $CrO(OH)_2$, CrO_2OH, CrO, CrO_2, CrO_3, ... [3]. From all, in oxidizing and H_2O-rich environments, $CrO_2(OH)_2$ is the dominant species and forms according to reaction R1 provided below, as it has been well documented in the literature [13-15]. In oxygen enriched and dry environments, the prominent species to form is CrO_3 (according to reaction R2), mainly above 1000 °C as previously mentioned [5]. The study of Berthod shows that CrO_3 could appear in industrial air environment in the temperature range of 1000-1300 °C [8]. In industrial applications such as turbine blades, solid oxyfuel cells, jet engines, super critical boilers components (reheater, header and main steam tubes), presence of water vapor is inevitable [15-18]. Accelerated Cr loss by reactions R1 and R2 from the oxide scale can create an acute problem for components with thin sections [19] and for lifetime prediction, leading to safety issues.

$$\frac{1}{2}Cr_2O_3 + H_2O + \frac{3}{4}O_2 = CrO_2(OH)_2\,(g) \qquad (R1)$$

$$\frac{1}{2}Cr_2O_3 + \frac{3}{4}O_{2(g)} = CrO_3(g) \qquad (R2)$$

Volatilization of chromia occurs simultaneously with the growth of the oxide scale. Tedmon first modeled the kinetics of chromium volatilization using the Wagner theory [20] by adding a negative term for scale thinning due to volatilization of compact Cr_2O_3 [21] as follows:

$$\frac{dx}{dt} = \frac{k_p}{2x} - k_v \qquad (1)$$

where x is the thickness (cm), t is time (s), k_p is the parabolic rate constant ($cm^2.s^{-1}$) and k_v is the volatilization rate ($cm.s^{-1}$). Initially, the mass gain variation related to the chromia growth is high compared to the mass loss of chromia due to volatilization. Then, the rate of oxide growth decreases as the oxide scale thickens until a critical thickness is reached (whose value depends on both kinetics of oxide growth and volatilization). Then, the mass loss is only a function of the volatilization rate. This behavior is called para linear and is often observed in chromia forming alloys in H_2O and O_2 rich environment [17,21,22]. Kinetics of species volatilization depends on composition of the alloy [23-25] and gas phase [10,26], gas velocity [9,27], time and exposure temperature [6,9].

Based on reaction R1, the higher the oxygen and H_2O partial pressures are, the larger the amount of volatilized Cr_2O_3. Indeed, high oxygen and water vapor partial pressures favor $CrO_2(OH)_2$ formation [11]. However, there exists an optimum H_2O/O_2 ratio at which the volatilization rate is maximum, as explained in [28]. In dry environments, the higher the oxygen partial pressure is, the larger is the amount of volatilized Cr_2O_3, according to R2.

The effect of temperature (500-800 °C) and gas velocity (0.02-13 cm/s) on chromia volatilization was studied in dry O_2 and O_2+40 vol. % H_2O by Asteman *et al.* on 304 L stainless steel [9]. They showed an increase in chromia volatilization at higher temperatures and gas velocities, leading to an early breakaway of the oxide scale. Similar observation was also made by Huczkowski *et al.* on alloy 625 exposed to wet air at temperatures ranging from 900 to 1000 °C [27]. Chromium content in the alloy also influences the components' lifetime. Higher chromium containing alloys are somewhat less sensitive to chromia volatilization because at higher temperatures, chromium can easily diffuse toward the surface, which prevents significant Cr depletion below the oxide scale and then breakaway, as shown by Asteman *et al.* for Fe-based alloys [25].

For 30 years, theoretical studies were conducted to better understand the complex interactions between the alloy surface composition and morphology, the environmental characteristics (gas temperature, composition, velocity) and the volatilization rate [1,6,9-12,23,25,29]. To calculate the volatilization rates, a common assumption is to assume that volatility is limited by the transport of the volatile species through a boundary layer in the gas phase and not by the chromia scale formation [15].

A first theoretical approach was proposed by Young and Pint in 2006 [1]. It was based on empirical correlations and analytical equations of mass transfer in flowing conditions, to estimate average volatilization rates around one sample. They analytically calculated the mass transfer coefficient for $CrO_2(OH)_2$ into flowing air-10% H_2O or steam for alloy 709 using empirical correlations. The calculated coefficient predicted correctly the overall rate of Cr loss as measured experimentally for one sample. Two years later, Holcomb used a similar approach to calculate the volatilization rates of chromia on Haynes 230, IN 625 and 304 L alloys exposed to a flowing mixture of air + (38% and 37 in vol.%) water at different gas velocities at 760 ℃ and compared with the experimental volatilization rates [15]. Similar analytical calculations were accompanied by experimental results by Huczkowski *et al.*[27] , Huang *et al.*[30] and Thublaor *et al.* [31] on In625 alloy, a NiCr coating and a 430 stainless steel coated by Mn-Co and Mn-Co-Cu oxides respectively. However, in all these studies, to calculate volatilization rates by Fick's law, the partial pressure of volatilizing species far away from the sample surface was assumed equal to zero. This hypothesis neglects the effect of gas phase enrichment by volatilizing species on volatilization rates. In 2009, Holcomb considered this effect for a hypothetical supercritical stream pipe under high pressure steam and showed with the help of analytical calculations that the enrichment of volatile species in the gas phase could reduce the volatilization rate by 80% in the conditions tested [16].

A second approach developed more recently consists in using Computational Fluid Dynamics (CFD) simulation tools to calculate local gas velocity and temperature distributions inside oxidation rigs of sapphire or SiC specimens [32-34]. Most of these studies [32,34] used the gas velocities obtained by CFD as input parameters for the empirical correlations of mass transfer to estimate average oxide recessions. Jacobson *et al.* [35] applied a different approach by estimating the volatile O_2 and SiO mass fluxes from the Hertz Knudsen Langmuir equation and the equilibrium vapor pressures of the volatile species, to obtain by CFD the local profiles of O_2 and SiO molar fraction around one SiO_2 coupon under laminar flow at 1650 °C. From these results and by using empirical correlations, they calculated local mass transfer coefficients and oxide recessions. However, once again the effect of local enrichment of the environment by volatile species on volatilization rate was not considered.

Experimental work by Asteman et al. (1999) [11] provided early qualitative evidence of vapor-phase accumulation effect on volatilization during high-temperature oxidation. In their study on 304L stainless steel at 600 °C in O_2+10%H_2O, they observed volatilization of chromium as $CrO_2(OH)_2(g)$, and always larger mass losses for upstream samples compared to downstream samples. This behavior was attributed to the accumulation of volatile species downstream, which they proposed could reduce the local driving force for further evaporation. Although they did not explicitly model species transport or quantify volatilization rates, their observations qualitatively captured the flow-dependent limitation of chromia volatilization. In our group, Oger *et al.* [22] experimentally showed the effect of gas phase enrichment by volatile species on volatilization rates, by testing three In625 coupons along a tubular horizontal rig at 900 °C under 74%N_2-18.5%O_2-7.5%H_2O (vol%) environment: the volatilization rate decreased from the inlet to the outlet positions of the samples in the test bench. They succeeded in predicting this behaviour by CFD calculation in a self-standing way. They indeed calculated the local profiles of gaseous species concentration inside the rig and of volatilization rate at each point of the coupons surface at 900 °C under laminar flow of $O_2/N_2/H_2O$ vapor. By using CFD, they showed that enrichment in $CrO_2(OH)_2$ of the gaseous environment resulting from the volatilization reaction of upstream samples causes decrease in the volatilization rate of downstream samples. The model predictions were validated by comparing the experimentally deduced and the CFD calculated volatilization constants for the three coupons.

In the study of Oger *et al.* [22], the inlet gas velocity was in the range of few cm/s, *i.e.* several orders of magnitude lower compared to those existing in most industrial conditions [36,37]. As previously mentioned, it has been shown experimentally that the volatilization rate increases with the inlet gas velocity [27,38]. Moreover, the sample geometry studied by Oger *et al.* was rather simple, as three disks of In625 in series were placed in line along the symmetry axis of the horizontal tubular rig. However, industrial parts like turbine blades or heat exchanger tubes have complex shapes, involving variable local gas velocities with potential recirculation loops and variable gas volumes in contact with the alloy surface, that could influence the local volatilization rates.

This is why, in the present work, a virtual oxidation rig with complex geometry has been simulated, allowing to reach local gas velocities up to 17 m/s at 900 °C around the sample surface. Such high velocities are close to those found in some industrial applications [36,37]. The objective is to understand the effect of local gas velocity, temperature and inlet gas composition on chromia volatilization using the experimentally validated CFD model developed by our group [22]. Simulations were made in wet air (74% N_2+18.5% O_2+7.5% H_2O in vol%) and pure O_2 environments at 800 and 900 °C. By this numerical study, the understanding of the effect of various hidden factors on volatilization which are difficult to evidence experimentally was refined.

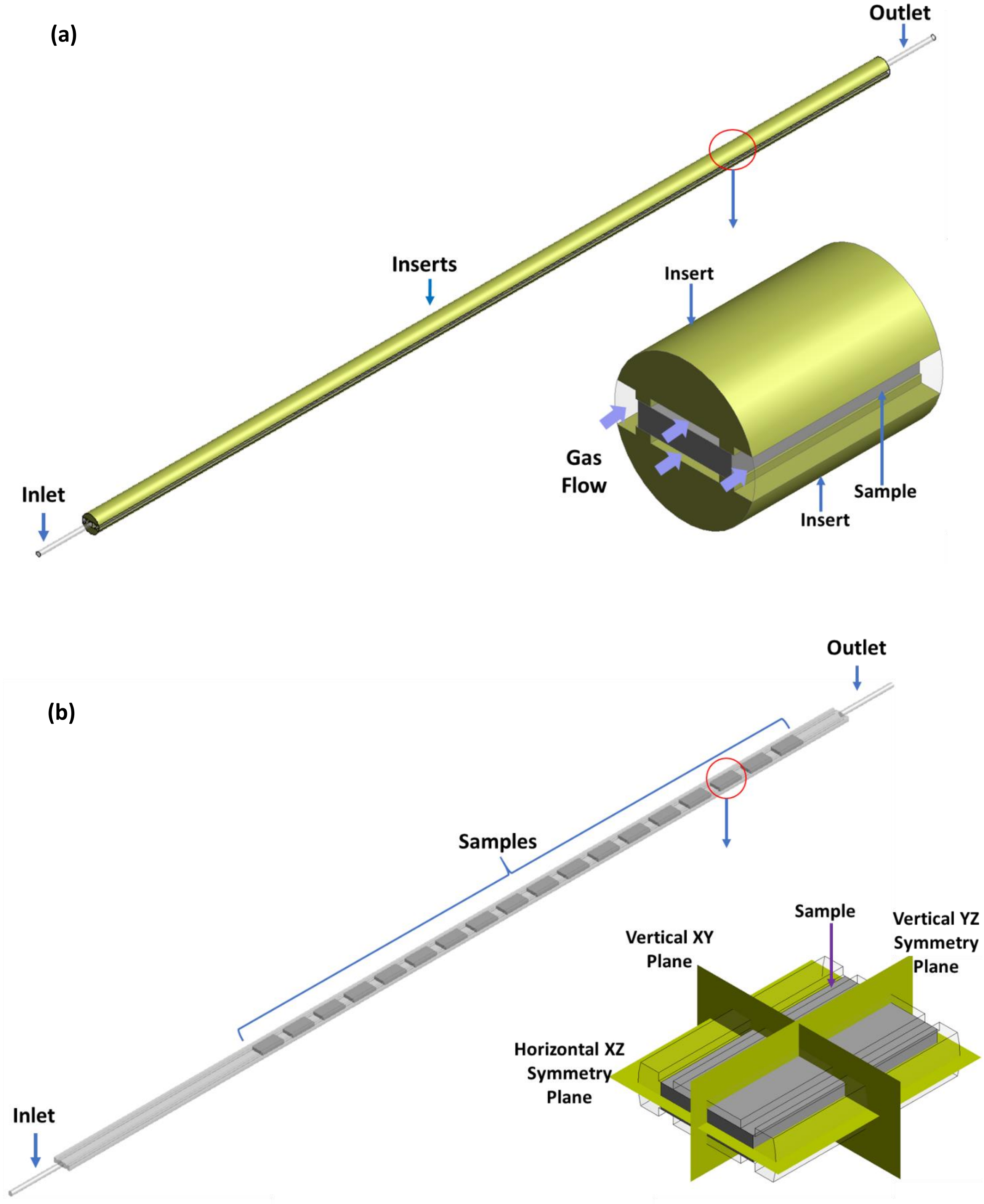

Fig. 1: 3D representation of (a) the whole rig with the inserts in yellow and zoom of the free volumes for gas flow around one sample (b) the samples position inside the rig and zoom around one sample to illustrate the various planes of work.

2. Method

2.1 Rig Design and sample arrangement

The volatilization phenomenon was simulated in a horizontal tubular rig represented by a 3D geometrical domain, as shown in **Fig. 1a**. The tube has a length of 91 cm and an inlet diameter of 1.9 cm. The gas inlet and outlet zones are constituted of small tubes of 6 cm in length and 0.48 cm in internal diameter. To reach high gas velocities, two inserts in quartz were placed all along the rig length, one on top of the samples and one below, as shown in the zoom of **Fig. 1a**. The hollow areas correspond to the regions open for gas flow around one sample. It is important to note that around each sample, the gaseous phase was divided into four separate volumes, as represented by the blue arrows in the zoom of **Fig. 1a**. In the regions between 2 samples, the flow converges in one open volume. With this configuration, the gas average velocity reached ~9 m/s at 900 °C around the sides of samples (close to the industrial application range) with a 5 slm inlet flow rate. To reproduce a sample arrangement during an oxidation test, 18 samples of chromia-forming alloys were placed horizontally inside the rig 23 cm from the rig inlet and separated from each other with a 1 cm distance, as illustrated in **Fig. 1b**. Samples were rectangular with 25.4 x 12.7 x 3.2 mm^3 dimensions. The zoom of **Fig. 1b** shows a magnified view of one sample to illustrate the two symmetry planes (XZ and YZ planes) and the vertical XY plane used to plot the simulation results.

Since the volume is symmetrical (along the YZ and ZX planes), only a quarter of the whole rig was simulated in 3D, as depicted in **Fig. 2a**. The sample arrangement is represented along the vertical YZ and horizontal XZ symmetry planes. Blue arrows illustrate the gas flow around the samples and in the free volume between the samples. A front view of the whole rig around one sample is provided in **Fig. 2b**, showing the cross-section of the inserts and the 4 volumes open for gas flow, two in contact with the top/bottom of the sample and the other two in contact with the sides of the sample. A magnified view of the rectangular region surrounded by a red dotted rectangle on **Fig. 2b** is given in **Fig. 2c,** showing a front view of the geometrical domain simulated by exploiting the two symmetry planes. The blue regions correspond to the two free volumes for gas flow around one sample.

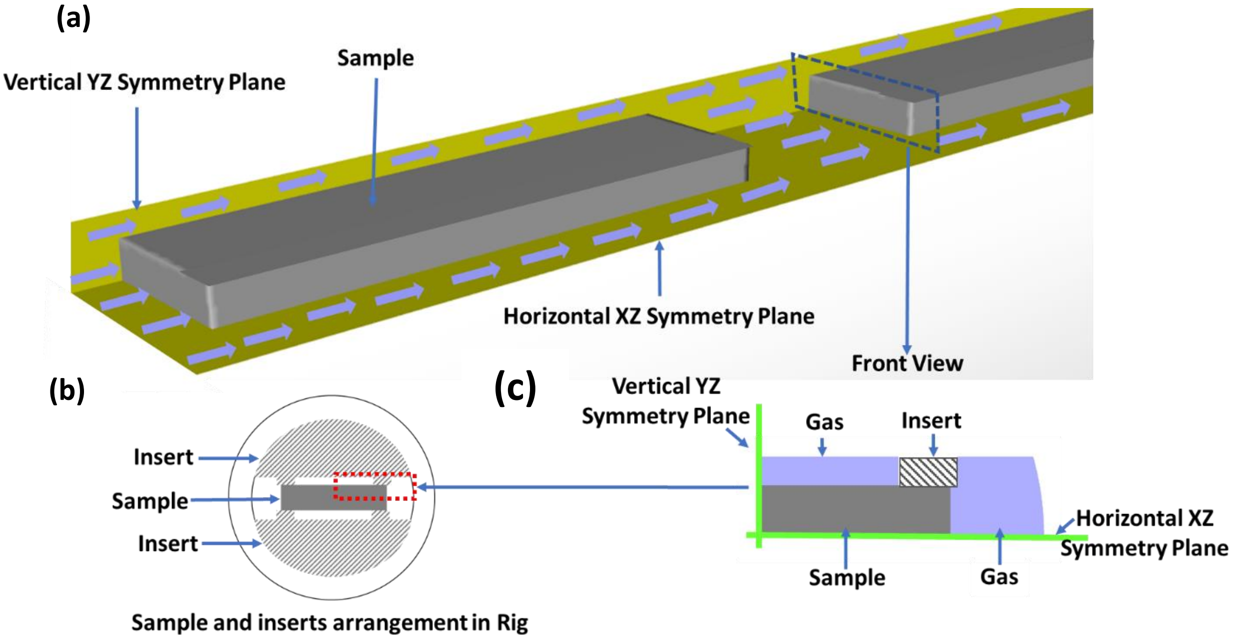

Fig. 2: (a) Magnified 3D view of a quarter of the rig along the YZ and XZ symmetry planes represented in green, (b) Cross section views (along the vertical XY plane) of the rig around one sample and (c) of a quarter of the rig (with a sample and 2 free volumes open for gas flow).

2.2 Model description

A CFD model was developed to simulate the transport phenomena existing in the gas phase and the formation of the $CrO_2(OH)_2$ and CrO_3 volatile species, according to reactions R1 and R2. The numerical simulations were run using the computer design software, mesh generator and CFD code FLUENT ANSYS® 2022. This code is a pressure-based, implicit Reynolds Averaged Navier Stokes solver employing a cell-centred finite volume scheme with second-order spatial accuracy. It is based on the discretization of the geometrical domain in elemental control volumes. These control volumes can be shaped as hexahedral, triangular, tetrahedral or hybrid meshes. The local gas velocity and temperature profiles are calculated by solving the mass conservation, momentum conservation, and thermal energy balance equations in each of the meshes. Solving the species conservation equations allow to calculate the local distribution of species molar fraction and the local volatilization rates. To simplify the calculations, several assumptions were made, such as steady-state conditions, laminar flow (Re < 1000), ideal gas, and incompressible gas flow thanks to low Mach number < 0.04 in the rig.

The FLUENT database was used to calculate the physical properties of O_2, N_2 and H_2O considering the gas kinetic theory using the Lennard-Jones parameters, i.e. the collision diameter (σ) and the characteristic energy of interaction (ε). The data for $CrO_2(OH_2)$ and CrO_3 were unavailable This is why, the values of □ and □ were taken equal to those used by Young and Pint [1] for $CrO_2(OH_2)$, as performed in the study of Oger *et al.* [22]. For CrO_3, the values used by Liu *et al.* [39] were considered (σ= 4.5Å and ε/k = 294.6, k being the Boltzmann's constant).

A 3D geometrical domain of 3,875,154 hexahedral cells were created representing only a quarter of the setup, as previously explained. Mesh refinement around the surface of the samples was made with a mesh size of 300 µm. Since two different gas volumes existed in contact with the sample surface, two symmetry planes (horizontal XZ and vertical YZ, as shown in **Fig. 1b**) were used to visualize the calculated results. The following boundary conditions were made:

- A mass flow rate of 5 slm (standard litres per minute) was imposed at the gas inlet. The gas temperature at the inlet and outlet was fixed to 25 °C. All the species mass fractions were imposed according to the composition of the inlet gas.
- A classical no slip condition was applied to all solid surfaces: sample surface, insert surface and rig wall. An isothermal zone was assumed for the rig wall between 6 cm and 97 cm from the rig inlet either at 800 or at 900 °C, as detailed in **Table 1**. Sample surfaces were supposed to be also isothermal and at the same temperature as the walls. The small inlet and outlet tubes were assumed to be at 25 °C, and a linear thermal evolution was supposed between the rig extremities and the central isothermal zone.
- The mass flow density of each species (except N_2) on the sample surface was calculated from the volatilization rates detailed below, using the stoichiometric coefficients of Reactions 1 and 2. The mass flow density was fixed to zero on the other surfaces, all considered as inert.
- A pressure outlet boundary condition was applied at the exit of the rig. The total pressure was fixed at atmospheric pressure (101,325 Pa). Zero diffusion flow was applied to other gas phase variables at the exit.

A user-defined function (UDF) was implemented into FLUENT to quantify the two volatilization reactions R1 and R2, which were considered as surface reactions. The calculation was made assuming that the sample surface was composed of only Cr_2O_3, i.e. the chromia activity a_{Cr2O3} was set equal to 1. It means that the chromia scale formation was not supposed to be a rate-limiting step (it was observed for Cr_2O_3-forming alloys that a chromia scale rapidly forms and covers the entire sample surface [28]). It is important to mention that the presence of Mn and Ti in significant amounts in the alloys could lead to spinel formation on the top of the oxide layer, which could reduce a_{Cr2O3} in the oxide layer and then the volatilization rate. However, it is worth noting that the effect of the chromia activity on volatilization is out of the scope of the present study. Once the volatile species form on the surface, diffusion through the gaseous phase was assumed to be the rate-limiting step. Therefore, the rate of volatilization was assumed to be equal to the diffusive flux of volatile species leaving the sample surface. The Fick's law (Equation 2) was used to calculate the flux density of each volatilizing species [22].

$$J_V = \frac{D_V}{\delta RT}(P_V^S - P_V^\infty) \qquad (2)$$

Where J_v is the flux density ($mol.m^2.s^{-1}$) of the volatile species (V= $CrO_2(OH_2)$ or CrO_3), D_V is the diffusion coefficient ($m^2.s^{-1}$) of the volatile species in the gas mixture, δ (m) is the characteristic length used by FLUENT to calculate the diffusive flux, R is the gas constant ($m^3.atm.mol^{-1}.K^{-1}$), T is the temperature (K), P_V^S and P_V^∞ are the partial pressures of volatile species (atm) respectively just above the sample surface and at a distance δ from the sample surface. The partial pressure P_V^S close to the sample surface was assumed to be equal to its equilibrium partial pressure calculated by Equations 3 and 4 for $CrO_2(OH)_2$ and CrO_3 respectively:

$$P_{CrO_2(OH)_2} = a_{Cr_2O_3}^{1/2} P_{H_2O} P_{O_2}^{3/4} exp\left(-\frac{\Delta G_1^0}{RT}\right) \qquad (3)$$

$$P_{CrO_3} = a_{Cr_2O_3}^{1/2} P_{O_2}^{3/4} exp(-\frac{\Delta G_2^0}{RT}) \qquad (4)$$

In the above equations, $a_{Cr_2O_3}$ is the chromia activity (considered equal to 1), P_{H_2O} and P_{O_2} are the partial pressures of H_2O and O_2 respectively (atm). ΔG_1^0 and ΔG_2^0 are the standard Gibbs energies of Reactions 1 and 2 respectively (J.mol^{-1}). ΔG_1^0 was taken equal to 106 kJ at 900 °C and 102 kJ at 800 °C per mole of $CrO_2(OH)_2$ using the thermodynamic calculations of Opila *et al.* [14]. For Reaction 2, standard Gibbs energy values were calculated using Equation 5, which was estimated using thermodynamic data given by Mittal *et al.* [40]:

$$\Delta G_2^0 = 265.\ 725 - 0.0525T \qquad (5)$$

ΔG_2^0 is in kJ per mole of CrO_3 and T in K. In Equation 2, J_V and P_V^{∞} are unknown parameters. The implementation of Equation 2 (one for $CrO_2(OH)_2$ and one for CrO_3) in a UDF, avoids any fitting of parameters, because FLUENT adjusts all the unknown values during its iterative procedure till convergence.

Table 1: Dimensions of the rig and respective wall temperatures

	Inlet tube wall	Tubular furnace	Outlet tube
Length (cm)	6	91	6
Diameter (cm)	0.48	1.9	0.48
Temperature (°C)	25	800 or 900	25

3. Results and Discussion

The simulations were carried out at 800 and 900°C with pure oxygen and 74%N_2-18.5%O_2-7.5%H_2O (vol%) environments considering a flow rate of 5 slm. By analysing the whole results obtained, it was found that at 900°C in wet environment (74% N_2+18.5% O_2+7.5% H_2O in vol.), the samples suffer the highest volatilization. Hence, results for this condition are presented in detail below. The key results about the influence of temperature and environment are then provided, before comparing volatilization rates obtained analytically and by CFD. The most important results of simulations at 800 °C are given in supplementary information (Fig. SI.1-SI.6).

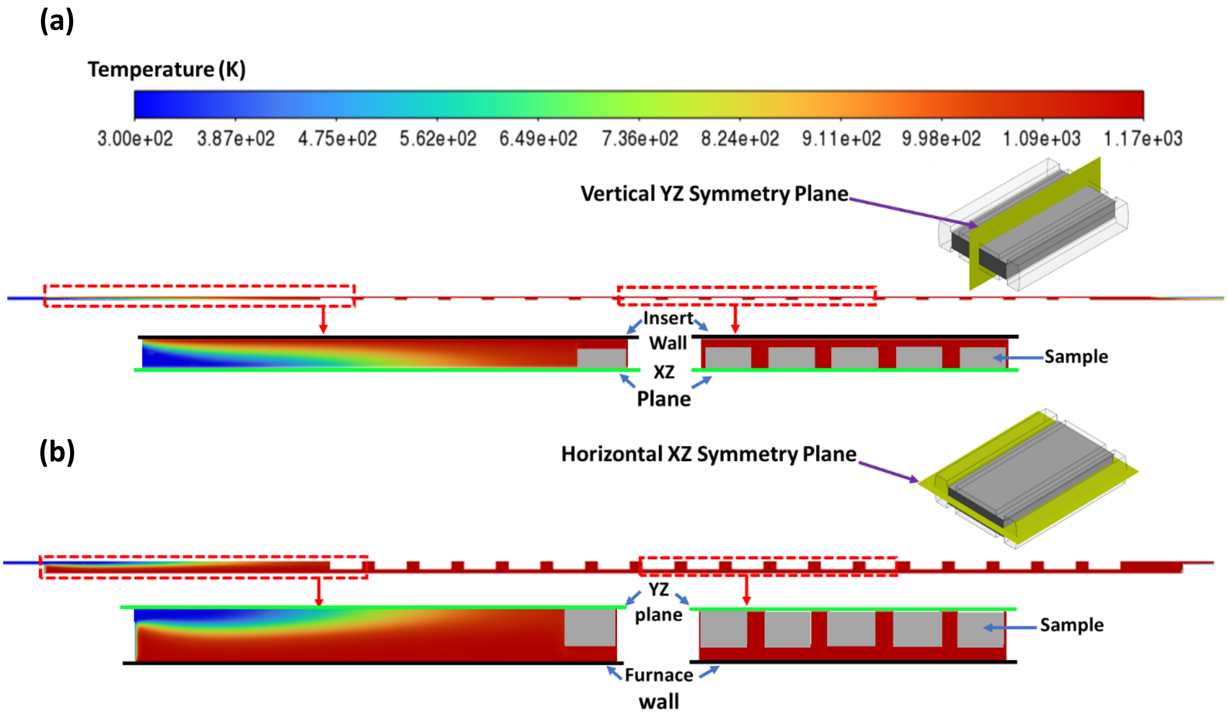

Fig. 3: Local temperature profile of the gaseous phase along (a) the vertical YZ plane and (b) the horizontal XZ plane at 900°C in 74% N_2+18.5% O_2+7.5%H_2O environment.

3.1 Temperature profile

Fig. 3a-b show the local temperature profiles of the gaseous phase along the YZ vertical and XZ horizontal symmetry planes respectively. Contours show a blue region depicting a lower temperature zone in both symmetry planes near the inlet of furnace. This is due to the inlet gas temperature fixed at 25°C, which results in the formation on a non-isothermal zone (27-723°C) of 23 cm in length from the inlet. The thermal profile is logically hotter near the furnace wall and presents a parabolic shape, characteristic of convective heat transfer existing in laminar flow. After this region, an isothermal zone (900°C) is observed up to the end of the furnace length that englobes all the samples.

3.2 Velocity Distribution

Fig.s 4a-d show the gas velocity profiles along the two symmetry planes. The highest velocity is observed in the outlet tube of the furnace (26 m/s), corresponding to hot gas flow in a zone of reduced cross-section area (Fig. S7). For the first three samples, the gas velocity profile is not fully established due to the presence of the inserts and samples modifying the gas flowing zones (**Fig.s 4a-b**). The velocity profile is fully established after the third sample (Fig. S8).

Fig. 4c provides a magnified view of the velocity profile along the vertical YZ symmetry plane around the 8th and the 9th samples from the inlet in the zone, where the velocity profile is fully established. The maximum velocity for the scale was set to 4.0 m/s to visualize the velocity variation around one sample. The gas velocity is the highest in the small free volume between the insert and the top of the sample surface (YZ plane); it is the lowest in the free volume between two samples because of the larger cross-sectional area open for the flow. Recirculation loops can be seen in the vector representation of gas velocity at the rear end of each sample. The gas velocity profile

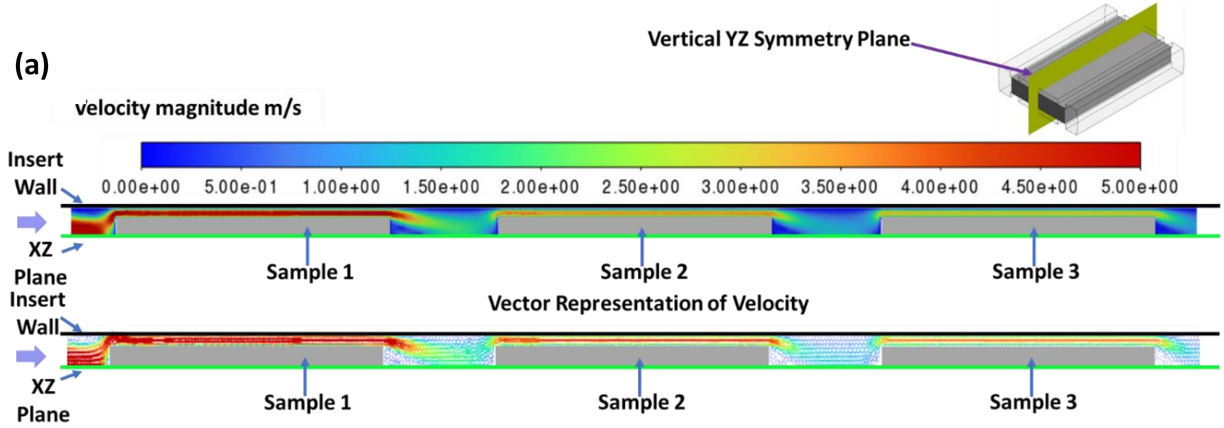

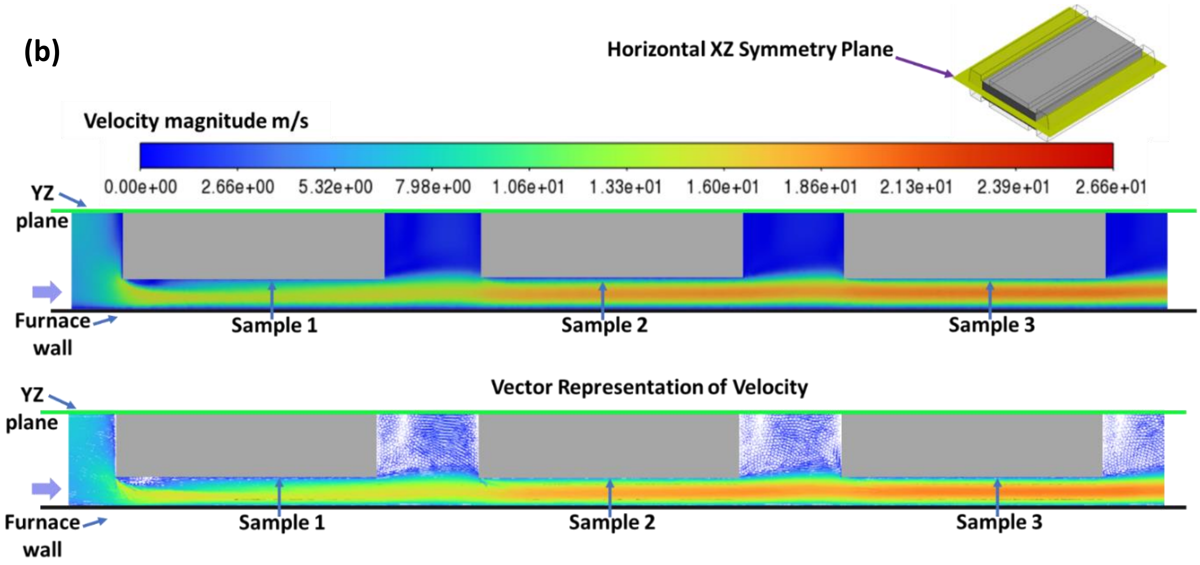

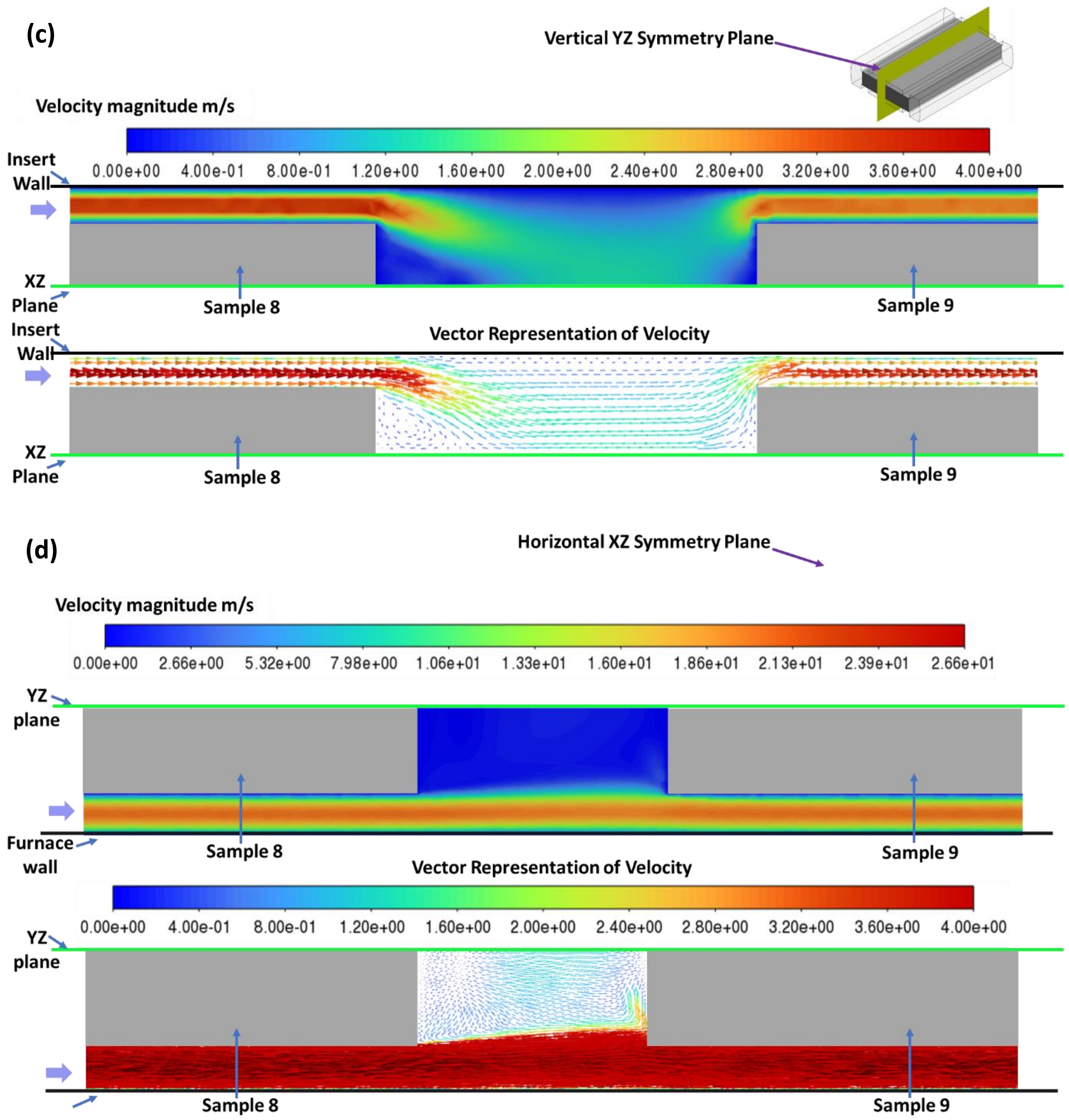

Fig. 4: Gas velocity distribution in (a,c) YZ and (b,d) XZ planes for an isothermal zone at 900 °C in 74%N_2+18.5%O_2+7.5%H_2O environment.

appears parabolic in all zones where flow is established, corresponding to a classical laminar flow. The maximum local gas velocity at the top of the sample's surface is close to 4 m/s.

Fig. 4d shows the gas velocity profile around the 8th and the 9th samples along the horizontal XZ symmetry plane. A high velocity zone is visible in the free volume on the sides of the samples; in the larger volume between two samples, the gas velocity is again logically lower. The maximum local gas velocity at the sides of the sample surface is around 17 m/s. Local gas velocity at the side of the samples is four times higher than at the top surface. A small part of the gas flow enters the free volume between samples due to the enlargement of the free section area, as seen in the vector representation of the gas velocity profile. The impact of this enlarged gas flow with the corner of the following sample produces recirculation loops of low gas velocity in the large volume. It is then clear that around each sample surface, low and high gas velocity regions are present due to differences in cross-sectional areas open for gas flow.

To have a better insight of this complex hydrodynamic behavior, **Fig. 5a** provides a 3D view of the gas velocity profiles around several samples (8, 9 and 10) which are represented in grey. Vertical XY cross-sectional planes were created to visualize the gas velocity variation in the free volume between two samples and around one sample side (**Fig. 5b-c**). The shaded region shows the position of the insert. Mass flow rates were calculated on several vertical cross-sectional planes along the furnace length, demonstrating the mass conservation in the simulations. Surface average gas velocities on these vertical planes were calculated by considering the mass flow rate divided by the gas density and area of the plane. The average gas velocity in the free volume between the samples is around 4 m/s (**Fig. 5b**). Around one sample, **Fig. 5c** shows that two separate gas velocity regions are formed. On the vertical plane at the top (named as Rectangle) and at the side (named as Rest) of the sample surface, the average gas velocity was around 2 and 10 m/s, respectively. As the Rectangular and Rest section areas are close to 9 and 22 mm^2, respectively, the corresponding mass flow rates are of 3.40×10^{-6} and 2.6×10^{-5} kg/s, respectively. This means that 88 wt.% of the total gas flow passes through the Rest region, thanks to the larger surface area open for gas flow. From the CFD simulation results, it was easy to calculate the Reynold number (Re) in these regions, considering their respective hydraulic diameter. The Re number for Rest and Rectangle is 261 and 22, respectively, confirming the laminar flow in both regions. In the following, it will be shown that the amount of gas volume interacting with the respective sample surface will influence the local evolution of the volatile species.

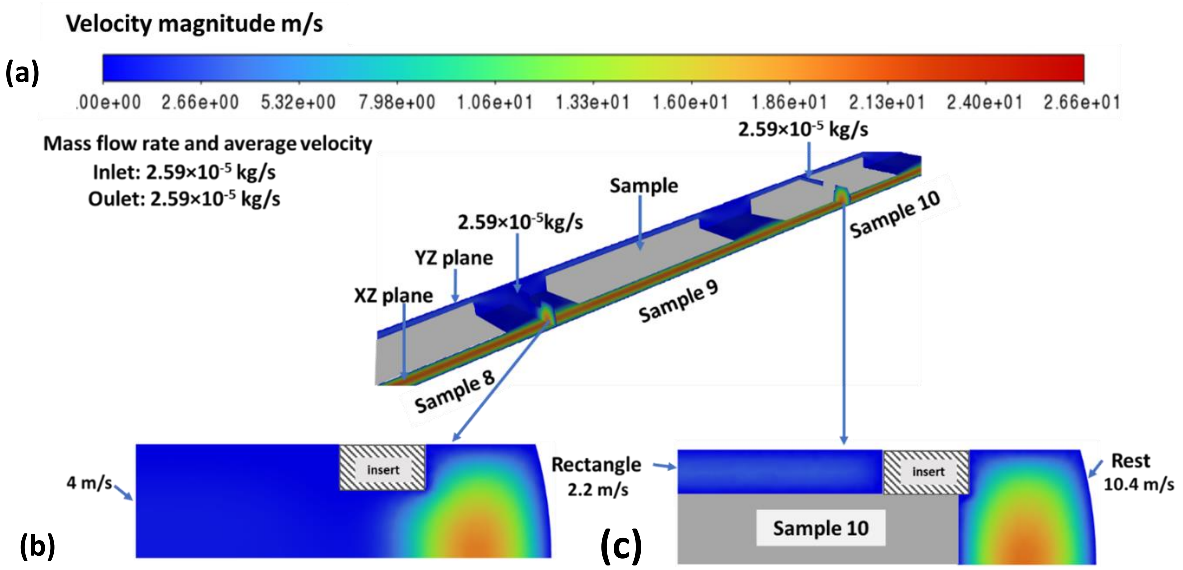

Fig. 5: (a) 3D view and mass flow rate calculation at 900 °C, Velocity distribution along XY vertical planes (b) in the free volume, (c) in the side gas volume around the sample in 74% N_2+18.5 % O_2+7.5%H_2O environment.

3.3 Gas Phase Evolution

Fig.s 6a-d detail the molar fraction profiles of the CrO_3 and $CrO_2(OH)_2$ species along the two-symmetry planes. In **Fig. 6a**, the CrO_3 molar fraction evolution along the vertical YZ symmetry plane is zoomed around the first two samples. It increases along the length of the first sample and reaches values close to the equilibrium (2.28×10^{-10}) in the free volume just after the second sample. Zoom around the last two samples (17th and 18th) shows complete CrO_3 saturation of the gaseous phase. It can be seen in **Fig. 6b** that the evolution of the $CrO_2(OH)_2$ molar fraction along the vertical YZ symmetry plane follows a similar trend as CrO_3 i.e. molar fraction values quickly reach equilibrium (3.74×10^{-7}) in the gaseous phase around the second sample. This saturation is due to the low gas velocity existing in the free volume between samples, leading to a poor removal of the volatile species. However, the molar fraction values for $CrO_2(OH)_2$ are three orders higher than those of CrO_3 everywhere in the gas phase of the rig from the first sample. This result agrees with the fact that $CrO_2(OH)_2$ is the predominant species in water rich oxidizing environments.

Fig.s 6c-d provide the CrO_3 and $CrO_2(OH)_2$ molar fraction profiles along the horizontal symmetry XZ plane. Zooming around the first two samples indicates that even if gradients appeared close to the sample surface, the core of the Rest zone where the gas velocity is high, remains poorly concentrated. On the contrary, the free volume between the first two samples where the gas velocity is low, is rapidly saturated. Zoom around the last two samples (17th and 18th) shows higher molar fractions of volatile species in the Rest zone, but it is still not fully saturated.

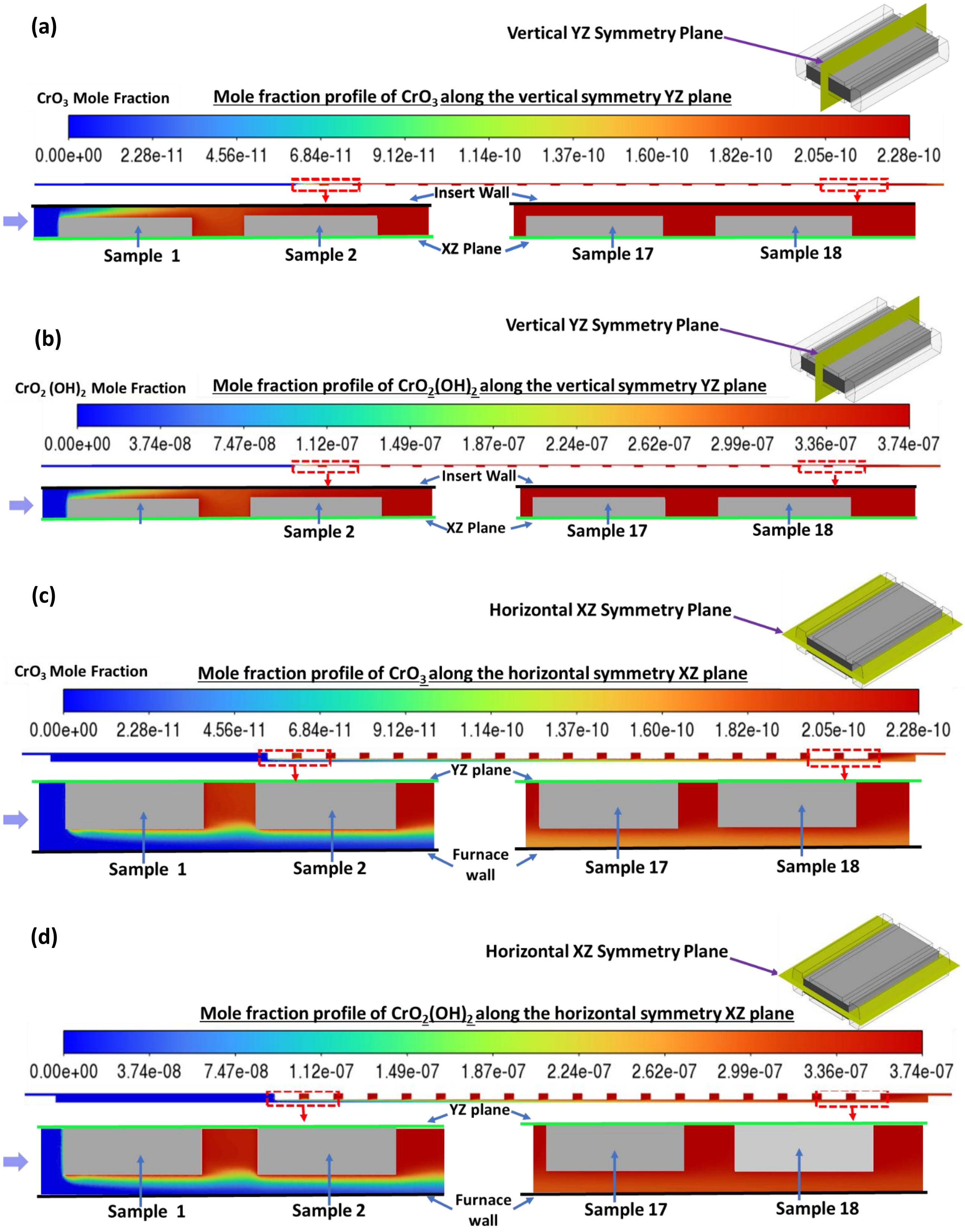

Fig. 6: Mole Fraction profiles of CrO_3 and $CrO_2(OH)_2$ along (a, b) vertical YZ, and (c, d) horizontal XY symmetry planes at 900 °C in 74% N_2+18.5% O_2+7.5% H_2O environment.

These whole results demonstrate that gaseous phase enrichment with volatile species is a complex function of the local gas velocity and of the ratio between the sample surface area S and the corresponding free volume V for gas flow (S/V ratio). As previously said, close to the samples' top/bottom surface, the average gas velocity on the vertical XY plane (Rectangle) was around 2 m/s for an open cross-sectional area of 9 mm^2, resulting in a lower volume of incoming flow passing through it.

The ratio of volume of gas interacting to the top surface area is 1:1 mm^{-1} (the surface to volume ratio was calculated by considering the top/side surface area of a sample and the respective gas volume interacting to it). For this zone, a lower gas velocity and a smaller volume of interaction resulted in an easier and quicker enrichment of volatile species in the gaseous phase. However, close to the sides' surface of the samples, the average velocity was around 10 m/s (Rest), for an open cross-sectional area of 22 mm^2 and a corresponding S/V ratio of 1:5 mm^{-1}. The higher velocity and larger volume of interaction resulted in lower enrichment in volatile species of the gas phase along the horizontal XZ symmetry plane.

3.4 Local volatilization rates

Performing CFD calculations allows to visualizing volatilization rates locally on each sample, which is not possible by experimental studies. **Fig. 7a-b** detail the local volatilization rates on the first three samples due to CrO_3 and $CrO_2(OH)_2$ formation. The shaded regions show the position of the insert in both figures. The inhomogeneity of volatilization rates around one sample can be easily seen. **Fig. 7a** shows the volatilization rate of Cr_2O_3 due to the formation of CrO_3 (reaction R2). On top/bottom surfaces of the first sample, it reaches a maximum value on the leading edge. When moving along the sample surface, it drastically decreases. For the next two samples, volatilization rates on the top/bottom surfaces are close to zero, which is expected since the gas is saturated in volatile species, as shown in **Fig. 6**. However, the sides of the sample are more prone to volatilization, in agreement with the mole fraction profiles of the volatile species previously discussed. The volatilization rate is the highest on the side surface of the first sample. On the side of the second and third samples, it decreases but it is 6 and 13 times higher than at the top/bottom surfaces of the respective samples.

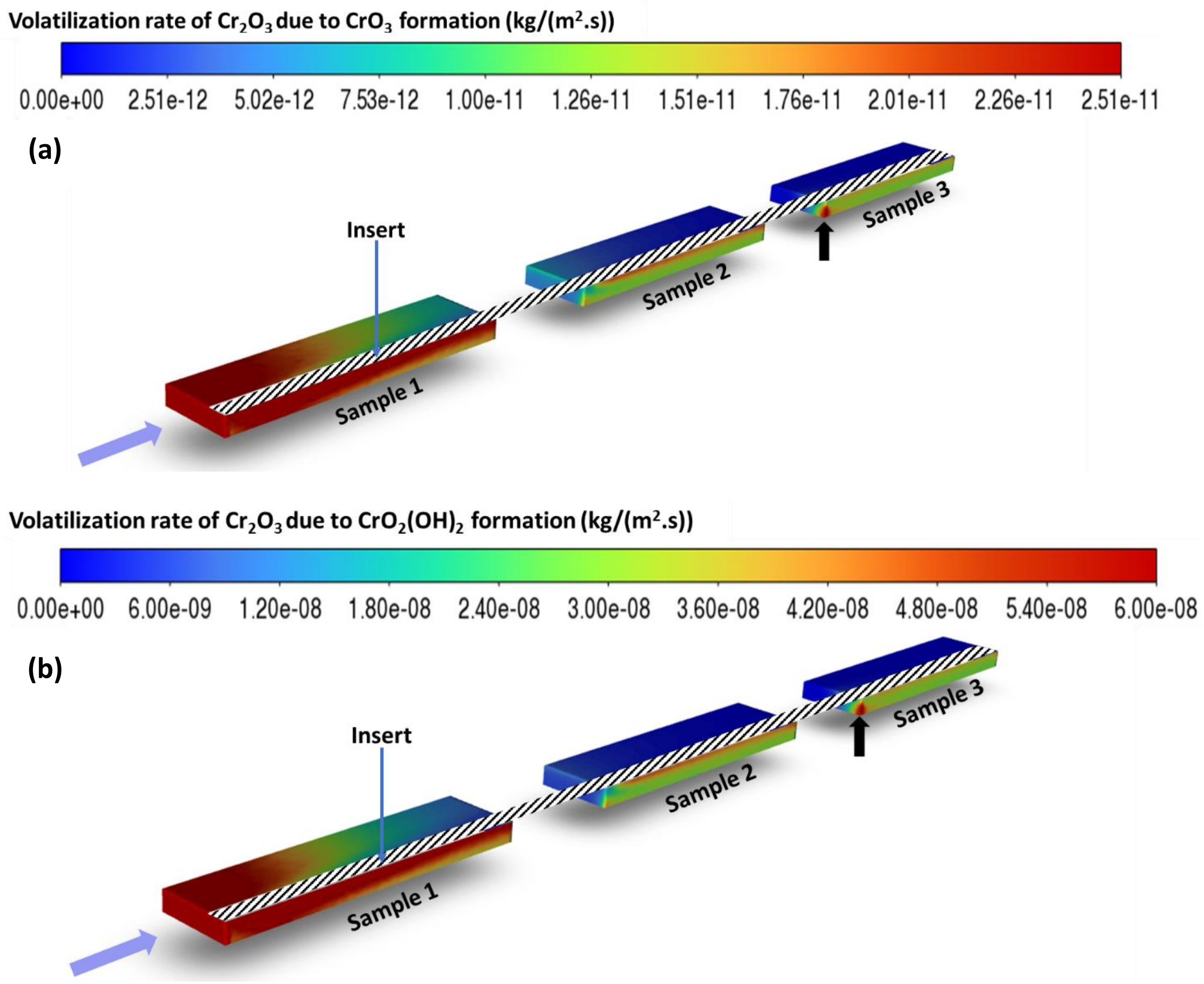

Fig. 7: Evolution of the volatilization rate of Cr_2O_3 on the first three samples at 900 °C due to (a) CrO_3 formation, (b) $CrO_2(OH)_2$ formation in 74% N_2+18.5% O_2+7.5%H_2O environment**.**

Overall, the volatilization rate decreases for consecutive samples. The front edge of the side of the second sample shows lower volatilization rates, because of the enriched gaseous phase with volatile species interacting with it (Fig. SI 9b). The top edge of sides of second sample also shows higher volatilization because the gaseous phase is less enriched around the edges (Fig. SI 9d). These heterogeneities in volatilization rate for the second sample are due to non-established gas velocity profiles (Fig.s S9a & c). Front edges (shown by black arrows in **Fig. 7a** and **b**) from third samples are prone to volatilization because the impacting gas flow previously described (**Fig. 4b**) leads to a lower thickness of diffusion layer and then to an easier removal of volatile species.

Fig. 7b shows the local volatilization rates of Cr_2O_3 due to the formation of $CrO_2(OH)_2$ (reaction R1) on the first three samples. The local inhomogeneities of volatilization rates on each sample are similar to those observed for CrO_3. However, the volatilization rate of Cr_2O_3 due to the formation of $CrO_2(OH)_2$ is three orders higher than the one due to the formation of CrO_3. The local inhomogeneities of volatilization rates have the same origins as those of the volatile species molar fractions, i.e. the differences in local gas velocity and gas volume in contact with each surface of individual samples. Such inhomogeneities in local volatilization rates on a given substrate have been recently demonstrated experimentally by Duthoit et al. [41].

For the top/bottom samples' surfaces, the gas velocity and volume of flow interacting with the surface are lower (Rectangle zone). Volatile species forming due to the interaction of the top surface to incoming flow, enriches the gaseous phase. This enrichment restricts the volatilization reactions (R1 and R2) on the top/bottom of the surface. It is clear now that the enrichment of the gaseous phase with volatile species depends on the local velocity of the gaseous phase. The lower the gas velocity, the larger the diffusion boundary layer, so the lower the mass flux and the more difficult the removal of volatilizing species. The other important parameter is the S/V ratio: as the cross-sectional area open for gas flow is lower, the gaseous volume interacting with the surface is also lower. Smaller interacting volumes around the sample surface require lesser amount of volatilizing species to get saturated, explaining why volatilization rates are lower for the top/bottom surfaces of the samples. This could be called "confinement effect". On the other hand, the sides of the samples are exposed to a larger interacting volume of gas flow and to high gas velocity (Rest zone). Enrichment till saturation of volatile species in larger volumes is difficult, and the high gas velocity in this region results in a continuous removal of volatile species.

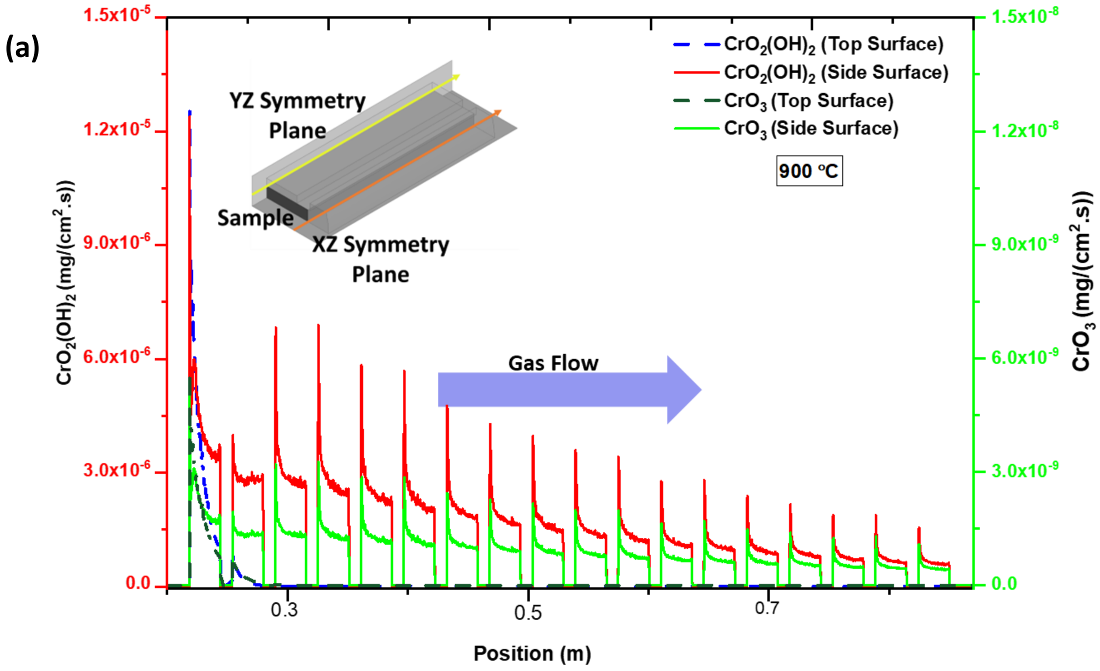

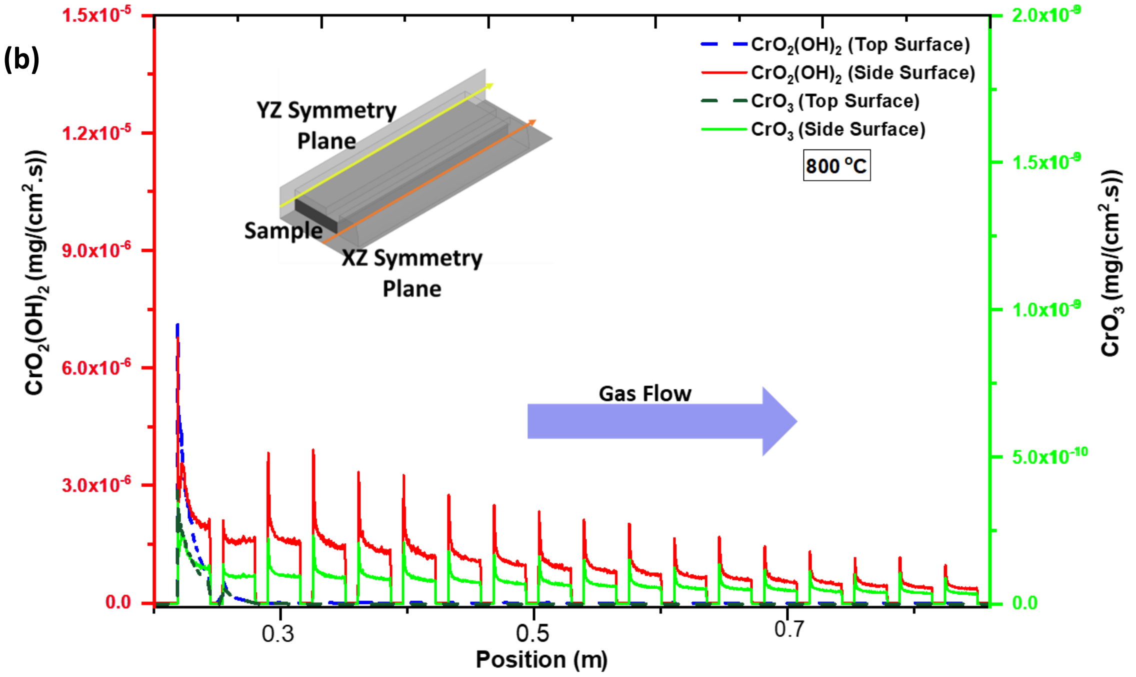

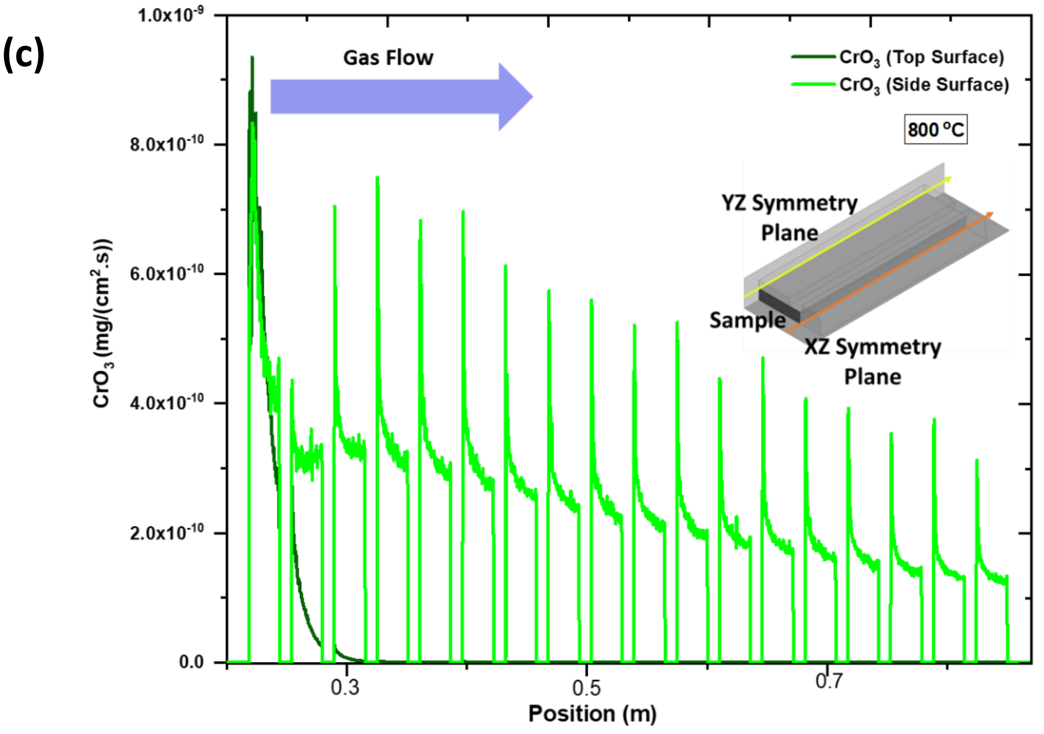

Fig. 8: Volatilization rates vs postion of the samples at (a) 900 °C, (b) 800 °C in in 74% N_2+18.5% O_2+7.5% H_2O environment and (c) 800°C in pure O_2 (volatilization rates were plotted along the pink (YZ symmetry plane) and orange (XZ symmetry plane) lines in the insets around the sample).

To have a complete overview, **Fig. 8a-c** show the local volatilization rates vs position of the samples along the rig at 800 and 900 °C in the wet air and pure O_2 environment. They were plotted along two lines corresponding to the intersection between the symmetry planes and the sample surface (yellow line for the top and orange line for the side of the sample, as shown in inset of **Fig. 8a-c**). Each crest represents the volatilization rate on the surface of individual samples (side/top). It appears clearly on **Fig. 8a** that at 900°C, the volatilization rate of Cr_2O_3 due to the formation of $CrO_2(OH)_2$ (left y-axis) is three orders higher than the one due to the formation of CrO_3 (right y-axis), as already observed on **Fig. 7**. For consecutive samples, the volatilization rates decrease rapidly, irrespective of the species and interaction volume. Volatilization rates on samples' top/bottom surface (vertical YZ symmetry) decrease rapidly after the first sample. They reach very low values after the second sample for both species, due to the confinement effect. However, higher volatilization rates, irrespective of species, were observed on the side surface of the samples (horizontal XZ symmetry planes), in agreement with **Fig. 7** results. Considering one sample, the volatilization rates are systematically the highest at the leading-edge and they decrease when moving along the sample length, irrespective of the volatile species.

Overall, the volatilization rates for the side of the second sample are lower than those of the third sample. It was attributed to the lower local velocity around the side of second sample, as already shown in **Fig. 4b**. This overview highlights the non-trivial and combined influences of (i) the presence of multiple samples, (ii) the local gas velocity surrounding them and (iii) the confinement or S/V ratio effect on the volatilization phenomena.

These results also confirm that gas velocity is a key parameter affecting volatilization. A higher gas velocity reduces the diffusion boundary layer thickness and favours the removal of volatile species, which increases the volatilization rate. At the same time, it promotes dilution of these species in the gas phase, lowering their partial pressure far from the surface and increasing the driving force for further volatilization. The final effect is the result of the balance between these mechanisms and the confinement effect previously explained. This is captured in the CFD model, which calculates the local gas velocity and gaseous species concentration profiles in the whole rig.

3.5 Effect of Temperature on Volatilization

To analyze the effect of temperature on volatilization rates of Cr_2O_3 due to CrO_3 and $CrO_2(OH)_2$ formation, a simulation was performed at 800 °C (**Fig. 8b**), to be compared to the one at 900 °C in 74% N_2+18.5% O_2+7.5% H_2O (vol%) environment (**Fig. 8a**). Similar trends for volatilization rates at 800 °C were observed than for samples exposed at 900 °C. However, overall volatilization rates were twice lower for samples maintained at 800 °C than those for samples at 900 °C. This result is logical since the equilibrium partial pressures of the two volatile species increase with temperature. Four times enhancement in Cr loss was shown experimentally by Spotorno *et al.* [9] for an increase in temperature from 650 to 850 ℃ for AISI 441 stainless steel. Similar observations were also made for 304L steel in the temperature range of 500-800 ℃ by Asteman *et al* [6], chromia volatilization was highest at 800 ℃.

3.6 Effect of atmosphere on volatilization

A simulation was made at 800 °C in pure O_2, to be compared to that in wet air at 800 °C. **Fig. 8c** shows the corresponding volatilization rates. The trends are similar as those observed for samples exposed at 800 and 900 °C in a wet air environment. However, the volatilization rates due to CrO_3 formation in a pure O_2 atmosphere are 3.5 times higher than those observed on samples exposed to a wet air environment at 800 °C. This is attributed to the higher partial pressure of O_2 in a pure O_2 atmosphere than in a wet air environment, leading to a higher concentration of CrO_3 as expected by reaction R2.

3.7 Analytical calculation and comparison of volatilization rates

In the previous sections, the influence of the local gas velocity and of the S/V ratio on the volatilization rates of $CrO_2(OH)_2$ and CrO_3 has been thoroughly analysed thanks to the results obtained by CFD. To complete the study, classical analytical expressions allowing to estimate overall volatilization rates were utilized [27,35]. As discussed by Jacobson *et al.* [35], the two approaches (CFD and analytical calculations) can hardly be compared, as they are very different in essence. For the analytical route, standard empirical correlations for mass transport from a flat plate are often used under isothermal conditions, allowing to obtain quite easily average volatilization rates. This approach cannot represent the phenomena existing around complex part shapes nor the impact of multiple samples. On the other hand, the CFD approach is much heavier to implement, as it involves 2D or 3D meshing of the rigs and the coupled resolution of the momentum, heat and mass transfer equations with the appropriate boundary conditions, considering the volatilization kinetics. However, CFD is the only way to get a complete picture of mass loss due to volatilization in flowing gas, as it allows to visualize the local profiles of gas velocity, temperature, volatile species molar fraction and volatilization rate, even in non-isothermal conditions and/or around single or multiple parts of complex shapes.

In the present work, for the first time, a comparison between average volatilization rates deduced from analytical and CFD calculations in different atmospheres and temperatures was made. Due to analytical approach limitation, only the first coupon of the rig was considered.

For the analytical approach, the mass flux density was calculated as follows, classically considering $P_V^{\infty} = 0$ (partial pressure of volatilizing species in upstream free gas):

$$J_V = h_v \left(\frac{P_V^S}{RT}\right) \qquad (6)$$

The empirical correlation to estimate mass transfer coefficients (h_v) at a flat plate interface volatilizing in a flowing gas in laminar conditions is described in various text books [42]. The average mass transfer coefficient (h_v in m/s) over a coupon of length L is given by:

$$h_v(L) = 0.664(Re)^{0.5}(Sc)^{0.33}\frac{D_v}{L} \qquad (7)$$

$$\text{with } Re = \frac{v_\infty \rho_\infty L}{\eta} \qquad (8)$$

$$\text{and } Sc = \frac{\eta}{D_v \rho_\infty} \qquad (9)$$

Where Re and Sc are the Reynolds and Schmidt dimensionless numbers, respectively, the characteristic length L (m) being the length of the plate. v_∞(m/s) and ρ_∞ (kg/m^3) are respectively the velocity and density of the gas in the free stream and η (Pa.s) is the dynamic viscosity of the flowing gas at the temperature T (K). Gas phase diffusivity (D_v) of a binary system was calculated using the Chapman-Enskog correlation [1].

Table 2: Comparison of average volatilization rates calculated analytically and by CFD for the first coupon in different atmospheres and temperatures.

Flow Rate= 5 slm	**Analytical volatilization rate (kg/m^{2}s)**	**CFD simulated volatilization rate (kg/m^{2}s)**
Environment: H_2O (7.5%) +O_2 (18.5%) +N_2 (74%); Volatilization due to $CrO_2(OH)_2$; 900 °C		
YZ Symmetry Plane *(Top Surface)*	3.85×10^{-8}	3.68×10^{-8}
XZ Symmetry Plane *(Side Surface)*	5.97×10^{-8}	6.64×10^{-8}
Environment: H_2O (7.5%) +O_2 (18.5%) +N_2 (74%); Volatilization due to CrO_3; 900 °C		
YZ Symmetry Plane *(Top Surface)*	2.05×10^{-11}	2.12×10^{-11}
XZ Symmetry Plane *(Side Surface)*	3.18×10^{-11}	3.33×10^{-11}
Environment: H_2O (7.5%) +O_2 (18.5%) +N_2 (74%); Volatilization due to $CrO_2(OH)_2$; 800 °C		
YZ Symmetry Plane *(Top Surface)*	2.26×10^{-8}	2.24×10^{-8}
XZ Symmetry Plane *(Side Surface)*	3.46×10^{-8}	3.85×10^{-8}
Environment: H_2O (7.5%) +O_2 (18.5%) +N_2 (74%); Volatilization due to CrO_3; 800 °C		
YZ Symmetry Plane *(Top Surface)*	1.58×10^{-12}	1.67×10^{-12}
XZ Symmetry Plane *(Side Surface)*	2.42×10^{-12}	2.48×10^{-12}
Environment: 100% O_2; Volatilization due to CrO_3; 800 °C		
YZ Symmetry Plane *(Top Surface)*	5.28×10^{-12}	5.91×10^{-12}
XZ Symmetry Plane *(Side Surface)*	8.0×10^{-12}	8.18×10^{-12}

Table 2 shows a comparison of the average volatilization rates obtained from CFD simulation and using the above analytical expressions at 900 and 800 °C under humid atmosphere and at 800°C under pure O_2. As the volatilization rates were the highest for the first sample of the rig in all cases, analytical calculations were made considering the velocity around the first coupon. As already explained, this is also the only coupon for which the analytical calculations can be made, since they cannot consider any gas phase enrichment due to upstream samples. Since incoming flow splits into two volumes around the sample, volatilization rates were calculated analytically considering surfaces exposed to either the top or the side of the samples. It is important to note that the velocity v_∞ in each volume was determined using FLUENT, because it was difficult to determine analytically this splitting

of gas flow. The gas velocities in the free stream were determined as integral mean values on the vertical cross-sectional plane (XY) around the first sample (in Rectangle and Rest areas). The volatilization rates obtained by CFD were averaged on the surfaces exposed to the gas flow passing through either the Rectangle zone (sample top) or the Rest region (sample side).

For the various studied cases in **Table 2**, the volatilization rates obtained from analytical expressions agree well with the average values deduced from the CFD simulations. This means that this analytical approach can be used confidently for configurations involving isothermal conditions, planar part geometries and only one sample. For more complex situations, the CFD route is mandatory. In particular, under laboratory-scale configurations where gas velocities are low, the diffusion boundary layer can become significantly thicker and reach the rig wall. Under these conditions, classical mass transfer models for flow over an open planar surface become inadequate, as the boundary layer may impinge upon the one corresponding to the heated wall, modifying the flow and species distribution. Naess et al. [43] illustrated this effect in their study of liquid silicon oxidation at 1500 °C, where a bulk gas velocity of 0.047 $m.s^{-1}$ inside a tube with an inner diameter of 5.2 cm resulted in significant deviation between analytical predictions and experimental results. The observed critical oxygen partial pressure for the transition from active to passive oxidation was between 2×10^{-3} and 5×10^{-3} atm, whereas theoretical estimates based on viscous flow regime mass transfer predicted a value of 8.6×10^{-3} atm—nearly twice the experimental result. They attributed this discrepancy to reduced geometry effect in the tubular furnace, where the boundary layer thickness was non-negligible relative to the tube diameter. The authors concluded that only CFD simulations, capable of capturing wall interactions and realistic velocity profiles, could reproduce the experimental volatilization behavior under such conditions.

4. Conclusions

In this work, the local gas phase evolution and volatilization rates existing in a virtual rig of oxidation of chromia forming alloys were simulated at 800 and 900°C in pure O_2 and in $O_2/N_2/H_2O$ atmospheres using a self-standing CFD model already validated experimentally. A complex design involving multiple samples in series associated to tubular inserts allowed to separate the gas flow into two channels, to reach local gas velocities up to 17 m/s, close to industrial practices. This design also permitted to create different ratios between the sample surface S and the corresponding free volume for gas flow V that revealed to have a marked effect on the volatilization rates.

The numerous results obtained revealed the combined and non-trivial influences of the gas phase enrichment from upstream samples, the local gas velocity and the S/V ratio. In particular, lower volatilization rates were observed for the sample surfaces exposed to low local gas velocities and a small volume of free gas due to rapid gas phase saturation related to a confinement effect, while sample areas exposed to high local gas velocities and a large volume of free gas were subjected to higher volatilization rates. In addition, the volatilization linked to the upstream samples contributed to saturate the gas phase surrounding the downstream samples, by such cancelling the volatilization rate for the most confined zones. The effects of temperature and of the O_2 concentration in the environment were also quantified on the local profiles of $CrO_2(OH)_2$ and CrO_3 volatile species mole fraction and Cr_2O_3 volatilization rate.

Moreover, by comparing overall volatilization rates analytically calculated with averaged ones deduced from the CFD results, this works demonstrates that the analytical approach can be used trustfully for simple configurations i.e. isothermal conditions and planar single sample. For more complex situations, the CFD route is mandatory.

Regarding industrial pieces of complex shape like airplane turbine blades or heat exchanger pipes, it is clear that more or less intense zones of volatilization and oxidation exist, depending on the local gas velocity and confinement effect that could be predicted and even mitigated by this CFD approach. As a perspective of this work, a combined experimental and numerical CFD study is in progress on the oxidation of chromia forming alloy samples of complex shape.

Acknowledgements

This research was funded by l'Agence Nationale de la Recherche (ANR), project ANR- 22-CE08-0026 organized in partnership with Air Liquide, Safran, LGC laboratory, Institut Jean Lamour laboratory and CIRIMAT laboratory. For open access, the author has applied a CC-BY public copyright licence to any Author Accepted Manuscript (AAM) version arising from this submission.

Authors Contributions

S.K. wrote the main manuscript text, prepared all the figures and tables, conducted the simulations and analysed the results with the supervision of B.C., H.V. and A.VP. H.V wrote the UDF used to simulate chemical reaction for gas phase simulation. B.C., A.VP, and H.V reviewed the manuscript.

Funding Open access funding provided by Institut National Polytechnique de Toulouse. Agence Nationale de la Recherche, ANR- 22-CE08-0026.

Declarations Competing Interests:

The authors declare that they have no known competing financial interests or personal relationships that could have appeared to influence the work reported in this paper.

References

1 Young DJ, Pint BA. Chromium volatilization rates from Cr 2 O 3 scales into flowing gases containing water vapor *Oxid. Met.* 2006;66:137-153.

2 Romedenne M, Pillai R, Dryepondt S, Pint BA. Effect of water vapor on lifetime of 625 and 120 foils during oxidation between 650 and 800° C *Oxid. Met.* 2021;96:589-612.

3 Ebbinghaus BB. Thermodynamics of Gas-Phase Chromium Species - the Chromium Oxides, the Chromium Oxyhydroxides, and Volatility Calculations in Waste Incineration Processes *Combust. Flame*. 1993;93:119-137.

4 McNallan M, Thongtem S, Liu J, Park Y, Shyu P. Corrosion of chromium containing alloys in non-steady state environments containing oxygen, carbon, and chlorine *Le Journal de Physique IV*. 1993;3:C9-143-C149-150.

5 Caplan D, Cohen M. The volatilization of chromium oxide *J. Electrochem. Soc.* 1961;108:438.

6 Spotorno R, Paravidino D, Delsante S, Piccardo P. Volatilization of chromium from AISI 441 stainless steel: Time and temperature dependence *Surf Coat Tech*. 2022;433:128125.

7 Ebbinghaus BB. Thermodynamics of Gas-Phase Chromium Species - the Chromium Chlorides, Oxychlorides, Fluorides, Oxyfluorides, Hydroxides, Oxyhydroxides, Mixed Oxyfluorochlorohydroxides, and Volatility Calculations in Waste Incineration Processes *Combust. Flame*. 1995;101:311-338.

8 Berthod P. Kinetics of high temperature oxidation and chromia volatilization for a binary Ni–Cr alloy *Oxid. Met.* 2005;64:235-252.

9 Asteman H, Svensson JE, Johansson LG. Evidence for chromium evaporation influencing the oxidation of 304L: The effect of temperature and flow rate *Oxid. Met.* 2002;57:193-216.

10 Asteman H, Svensson J-E, Johansson L-G. Oxidation of 310 steel in H2O/O2 mixtures at 600 C: the effect of water-vapour-enhanced chromium evaporation *Corros. Sci.* 2002;44:2635-2649.

11 Asteman H, Svensson J-E, Johansson L-G, Norell M. Indication of chromium oxide hydroxide evaporation during oxidation of 304L at 873 K in the presence of 10% water vapor *Oxid. Met.* 1999;52:95-111.

12 Asteman H, Svensson JE, Norell M, Johansson LG. Influence of water vapor and flow rate on the high-temperature oxidation of 304L; Effect of chromium oxide hydroxide evaporation *Oxid. Met.* 2000;54:11-26.

13 Kim Y, Belton G. The thermodynamics of volatilization of chromic oxide: Part I. the species CrO 3 and CrO 2 OH *Metallurgical Transactions*. 1974;5:1811-1816.

14 Opila EJ, Myers DL, Jacobson NSet al. . Theoretical and experimental investigation of the thermochemistry of CrO2(OH)2(g) *J. Phys. Chem. A*. 2007;111:1971-1980.

15 Holcomb GR. Calculation of reactive-evaporation rates of chromia *Oxid. Met.* 2008;69:163-180.

16 Holcomb GR. Steam oxidation and chromia evaporation in ultra-supercritical steam boilers and turbines *ECS Transactions*. 2009;16:81.

17 Buscail H, Rolland R, Issartel Cet al. . Effects of water vapour on the oxidation of a nickel-base 625 alloy between 900 and 1,100° C *Journal of materials science*. 2011;46:5903-5915.

18 Meschter PJ, Opila EJ, Jacobson NS. Water vapor–mediated volatilization of high-temperature materials *Annual Review of Materials Research*. 2013;43:559-588.

19 Romedenne M, Pillai R, Dryepondt S, Pint B. Oxidation Lifetime Modeling of 625 and 120 Foils After Long-term Exposure in Flowing Air+ 10% H 2 O at 700 and 800∘ C *Oxid. Met.* 2022;98:305-324.

20 Wagner C. Beitrag zur theorie des anlaufvorgangs *Z. Phys. Chem.* 1933;21:25-41.

21 Tedmon C. The effect of oxide volatilization on the oxidation kinetics of Cr and Fe-Cr alloys *J. Electrochem. Soc.* 1966;113:766.

22 Oger L, Vergnes H, Caussat B, Monceau D, Vande Put A. Fluid dynamic simulation of CrO2(OH)2 volatilization and gas phase evolution during the oxidation of a chromia forming alloy *Corros. Sci.* 2022;203:110306.

23 Berthod P, Allègre F, Kretz E. Influence of titanium on the high temperature oxidation and chromia volatilization of ternary Ni–Cr–C alloys *Oxid. Met.* 2016;86:581-595.

24 Conrath E, Berthod P. Kinetics of high temperature oxidation and chromia volatilization for HfC-containing nickel-based alloys *Oxid. Met.* 2014;81:393-405.

25 Asteman H, Svensson J-E, Johansson L-G. Effect of water-vapor-induced cr vaporization on the oxidation of austenitic stainless steels at 700 and 900° C: Influence of Cr/Fe ratio in alloy and Ce additions *J. Electrochem. Soc.* 2004;151:B141.

26 Mahboubi S, Zurob HS, Botton GA, Kish JR. Effect of water vapour partial pressure on the chromia (CrO)-based scale stability *Can. Metall. Q.* 2018;57:89-98.

27 Huczkowski P, Lehnert W, Angermann HHet al. . Effect of gas flow rate on oxidation behaviour of alloy 625 in wet air in the temperature range 900–1000 C *Mater. Corros.* 2017;68:159-170.

28 Young DJ *High temperature oxidation and corrosion of metals*. City: Elsevier; 2008.

29 Zaplatynsky I. Volatilization of Oxides during Oxidation of Some Superalloys at 1200-Degrees-C *Oxid. Met.* 1977;11:289-305.

30 Huang W, Huang T, Song Pet al. . CrO2 (OH) 2 volatilization rate and oxidation behavior prediction of the NiCr coating in air-H2O environment at 650℃ *Corros. Sci.* 2021;182:109303.

31 Thublaor T, Chandra-ambhorn S. High temperature oxidation and chromium volatilisation of AISI 430 stainless steel coated by Mn-Co and Mn-Co-Cu oxides for SOFC interconnect application *Corros. Sci.* 2020;174:108802.

32 Ridley MJ, Opila EJ. Quantitative evaluation of (0001) sapphire recession in high-temperature high-velocity steamjet exposures *J. Eur. Ceram. Soc.* 2022;42:631-637.

33 Sharma AK, Sagawa W, Ahmed Z, Nishimura Y, Okamoto K. Integrated experimental assessment and validation of oxidation with real-scale SiC fuel compact in HTGR *Int. J. Heat Mass Transfer*. 2024;220:124930.

34 Golden RA, Opila EJ. A method for assessing the volatility of oxides in high-temperature high-velocity water vapor *J. Eur. Ceram. Soc.* 2016;36:1135-1147.

35 Jacobson NS, Kuczmarski MA, Kowalski BA. Vaporization of Protective Oxide Films into Different Gas Atmospheres *Oxid. Met.* 2020;93:247-282.

36 Bender M, Rakowski J, Lipschutz M. Validation of ATI 20-25+ Nb™ Alloy at 50,000 Hours in the Recuperator of a Gas Turbine Engine. *Turbo Expo: Power for Land, Sea, and Air*, City; American Society of Mechanical Engineers;2012:479-487.

37 Al-Masri A, Peksen M, Blum L, Stolten D. A 3D CFD model for predicting the temperature distribution in a full scale APU SOFC short stack under transient operating conditions *Appl Energ*. 2014;135:539-547.

38 Froitzheim J, Ravash H, Larsson E, Johansson LG, Svensson JE. Investigation of Chromium Volatilization from FeCr Interconnects by a Denuder Technique *J. Electrochem. Soc.* 2010;157:B1295-B1300.

39 Liu TK, Bautista RG. Prediction of the Chromium-Oxide Oxidation Rate from the Equilibrium-Constants and the Mass-Transfer Coefficients at High-Temperatures *Oxid. Met.* 1981;15:277-286.

40 Mittal A, Albertsson GJ, Gupta GS, Seetharaman S, Subramanian S. Some Thermodynamic Aspects of the Oxides of Chromium *Metallurgical and Materials Transactions B-Process Metallurgy and Materials Processing Science*. 2014;45:338-344.

41 Duthoit G, Vande Put A, Caussat B, Vergnes H, Monceau D. Influence of water vapor and local gas velocity on the oxidation kinetics of In625 at 900 C: experimental study and CFD gas phase simulation *High Temperature Corrosion of Materials*. 2024;101:1513-1526.

42 Gaskell DR, Krane MJM *An introduction to transport phenomena in materials engineering*. City: CRC Press; 2024.

43 Næss MK, Young DJ, Zhang J, Olsen JE, Tranell G. Active oxidation of liquid silicon: Experimental investigation of kinetics *Oxid. Met.* 2012;78:363-376.